RESEARCH ARTICLE

NANO · MICRO small

www.small-journal.com

Flash Joule Heating Synthesis of Nitrogen-Rich Defective G-C_3N_4 for Highly Efficient Photocatalytic Hydrogen Evolution

Jiawei Xiao, Yun Chen, Chuhao Cai, Shengbao Lai, Liang Cheng, Junjie Zhang, Wenxuan Zhu, Yuanhui Guo, Maoxiang Hou, Li Ma, Wanqun Chen, Xin Chen, and Ching-Ping Wong*

Seeking renewable energy solutions that are sustainable and environmentally friendly is a critical contemporary research imperative. This paper presents a flash Joule heating approach to prepare high-performance nitrogen-rich defective graphitic carbon nitride (g-C_3N_4) for hydrogen production by photocatalytic water splitting at ultralow cost. By leveraging the rapid heating and cooling capabilities of flash Joule heating, and using melamine as the sole precursor, defects are introduced and precisely regulated while preserving the structural integrity of as-synthesized prepared g-C_3N_4. By tuning the processing parameters, the band structure of g-C_3N_4 can also be optimized, which can significantly suppress electron-hole recombination and substantially enhance its photocatalytic hydrogen evolution from splitting water. As a result, a hydrogen evolution rate of 16936.5 µmol h^{-1} g^{-1} for Pt/g-C_3N_4 is achieved, which is comparable to the leading benchmarks in the field. Through a life cycle assessment (LCA) and a cradle-to-gate techno-economic assessment (TEA), this method reduces costs to 1/12, energy consumption to 1/23, and CO_2 emissions to less than 1/8 of those associated with the thermal polymerization approach under equivalent conditions. These results underscore the exceptional advantages of the developed method in cost-effectiveness and environmental sustainability, offering a robust scientific foundation for the industrial-scale production of g-C_3N_4-based photocatalysts.

1. Introduction

Graphitic carbon nitride (g-C_3N_4) based photocatalysts have attracted considerable attention in both academia and industry because of their notable advantages, including a large specific surface area derived from 2D structure, strong visible-light absorption, and well-matched conduction band alignment.[1] However, g-C_3N_4 is limited by the rapid recombination of photogenerated electron-hole pairs and an inadequate surface reaction rate, which results in photocatalytic performance that is considerably below the requirements and expectations for widespread practical application.[2–4]

Defect modulation has become a pivotal strategy for enhancing the photocatalytic hydrogen evolution (PHE) activity of g-C_3N_4 in visible-light-driven water splitting. Among the various methods for defect modulation, thermal treatment has become a key technique for precise defect engineering, facilitating the controlled generation of atomic defects with distinct coordination states in g-C_3N_4. By fine-tuning critical parameters such as temperature and treatment duration, this method enables the manipulation of defect type and concentration,[5–8] thereby facilitating the modulation of the energy band structure,[9,10] and electronic properties and photocatalytic activity[11] of a material. Owing to its high degree of controllability and adaptability in introducing nitrogen defects, thermal treatment has attracted substantial attention in defect modulation research.

J. Xiao, Y. Chen, C. Cai, L. Cheng, J. Zhang, W. Zhu, Y. Guo, M. Hou, L. Ma, X. Chen
State Key Laboratory of Precision Electronic Manufacturing Technology and Equipment
School of Electromechanical Engineering
Guangdong University of Technology
Guangzhou 510006, China
E-mail: chenyun@gdut.edu.cn

The ORCID identification number(s) for the author(s) of this article can be found under https://doi.org/10.1002/smll.202503335

DOI: 10.1002/smll.202503335

S. Lai
Ganzhou Aoketai Tools Technology Co., Ltd
Industrial Third Road, Economic and Technological Development Zone
Ganzhou 341003, China

W. Chen
Suzhou Maxwell Technologies Co.
No. 228, Ludang Road, Wujiang District, Suzhou, Jiangsu 215200, China

C.-P. Wong
School of Materials Science and Engineering
Georgia Institute of Technology
Atlanta, GA 30332, USA

To achieve precise control over the crystal structure and defect configurations of carbon nitride materials, Liu et al. developed a two-step, molten-salt-assisted method for poly (triazine imide) (PTI) synthesis. The synthesized PTI was noted to exhibit an extended π-conjugated and highly crystalline framework with a well-ordered structure, which can promote the extensive exposure of surface pyridinic nitrogen species, thus considerably enhancing electron delocalization and facilitating density optimization.[12] Thermal treatment has become a key strategy in defect engineering because it enables the direct introduction of various intrinsic defects through high-temperature calcination without the use of chemical etchants. Elevated thermal energy accelerates bond cleavage and facilitates the migration of atoms out of the lattice, resulting in vacancy-type defects.[13,14] Di[15] and Zhang[16] applied two-step thermal treatments to introduce a high concentration of surface carbon vacancies into nanosheets exfoliated from bulk g-C_3N_4. These vacancies were introduced because they are beneficial for enhancing photocatalytic activity. Zhou et al.[17] directly incorporated 2-aminopyridine molecules at the edge of the carbon nitride framework to produce nitrogen-defect-rich carbon nitride.

However, due to its narrow thermal stability range, melamine, which is a widely adopted precursor for the synthesis of g-C_3N_4, undergoes polymerization into g-C_3N_4 at temperatures above 520 °C but decomposes rapidly when the temperature exceeds 650 °C.[18] This pronounced temperature sensitivity, coupled with the prolonged heating durations and the concurrent release of gases, considerably increases the difficulty of achieving precise control over the final product. Considering the limitations imposed by thermal stability, extended processing durations, and energy inefficiency, conventional thermal treatment methods face inherent challenges in scalability. Consequently, the development of cost-effective defect engineering strategies for producing superior-grade g-C_3N_4 for highly efficient photolysis has become a pivotal focus in current research endeavors.

Zhang et al. used a high-temperature to rapidly treatment method to rapidly eliminate nitrogen atoms from g-C_3N_4, by increasing the temperature to 800 °C at a rate of 600 °C min^{-1} and maintaining this temperature for 15 min before the annealing. This approach resulted in g-C_3N_4 materials with excellent PHE performance.[19] Lin et al. applied thermal treatment to melamine-derived g-C_3N_4 in a vacuum environment, which not only enhanced its thermal stability but also ensured its purity.[20] Vinu et al. demonstrated that g-C_3N_4 with different nitrogen contents and molecular structures could be synthesized by carbonizing nitrogen-rich precursors at various pyrolysis temperatures, which could lead to the formation of structural features with N-rich active sites.[21] Several studies have attempted to optimize the characteristics of g-C_3N_4 through the modulation of the annealing process. To optimize the effects of nitrogen vacancies, Longobardo et al. extended the annealing duration, which helped reduce the material bandgap.[22] Similarly, Kubanaliev et al. performed annealing at a controlled temperature to improve the yield of the process.[23] Despite these advances, the precise influence of processing temperature on the formation of nitrogen vacancies and their subsequent effects remains unclear. Moreover, further research is warranted to develop a cost-effective and energy-efficient approach for industrial-scale g-C_3N_4 production.

Tour et al. pioneered the use of flash Joule heating for the efficient fabrication of graphene. They have established a synthesis, within a fleeting duration of less than 1 s (<1 s) that generates a substantial amount of Joule heat, achieving temperatures approaching 3000 K, thereby synthesizing high-yield flash graphene.[24] This innovative approach is not limited to traditional carbon sources, it extends to a diverse array of sustainable, renewable, and waste-derived carbon materials.[25–28] On the basis of the insights, Hu presented a novel Joule-heat-based methodology for the programmable heating and quenching of CH_4,[27] which allows the dynamic control of thermal chemical reactions, and programmable fashion, heralding a new frontier in the controlled decomposition of hydrocarbons. The aforementioned methodology can also be used to recycle waste glass-fiber-reinforced plastics into silicon carbide, effectively mitigating the challenges of environmental contamination and resource wastage.[29]

In this study, we have innovatively applied flash Joule heating in the synthesis of g-C_3N_4 to achieve a precise defect modulation (**Figure 1**). By leveraging the high-speed heating and cooling capabilities of flash Joule heating, this method generates a high-temperature shock that efficiently converts melamine into nitrogen-rich defective g-C_3N_4 with a porous layered structure within a remarkably brief duration (≈72). The proposed method was used to prepare the Pt/g-C_3N_4-625 achieves an impressive hydrogen evolution rate of 16936.5 μmol h^{-1} g^{-1}, which is comparable to the leading benchmarks in the field. Under conditions of comparable H_2 conversion efficiency and identical yield, the cost of this method is only 1/12 that of the thermal polymerization method, energy consumption is reduced to 1/23, and CO_2 emissions are less than 1/8. These results demonstrate clear advantages in terms of cost-effectiveness and environmental sustainability, offering a pivotal reference for the industrial-scale synthesis of carbon-nitride-derived photocatalysts.

2. Results and Discussion

The specific steps for synthesizing g-C_3N_4-x (x represents the synthesis temperature in °C, and $x = 525, 550, 575, 600, 625, 650$) from melamine on carbon paper using the flash Joule heating method are outlined in **Figure 2a**. First, the melamine as the sole precursor is moistened with deionized water to create an aqueous slurry, which is loaded onto carbon paper. This paper is then placed in a vacuum chamber maintained at a base pressure of 10^{-7} Pa. Subsequently, the precursor is subjected to high-temperature impulse shock heating via the Joule heating effect. By programming key parameters including heating temperature, pulse duration, and temperature change rate, the synthesis process is precisely controlled, allowing for stringent regulation of the reaction process temperature, which facilitates the attainment of rigorous control in both spatial and temporal dimensions and is essential for ensuring the accurate supply of energy and the stability of the reaction kinetics. In contrast to traditional heating methods, the proposed method requires less time and thus significant reduction in the energy consumption of the process. Figure 2a-II illustrates the processing temperature variation during a complete high-temperature impulse shock cycle, which comprises six subcycles and is completed within 72 s. The maximum processing temperature is

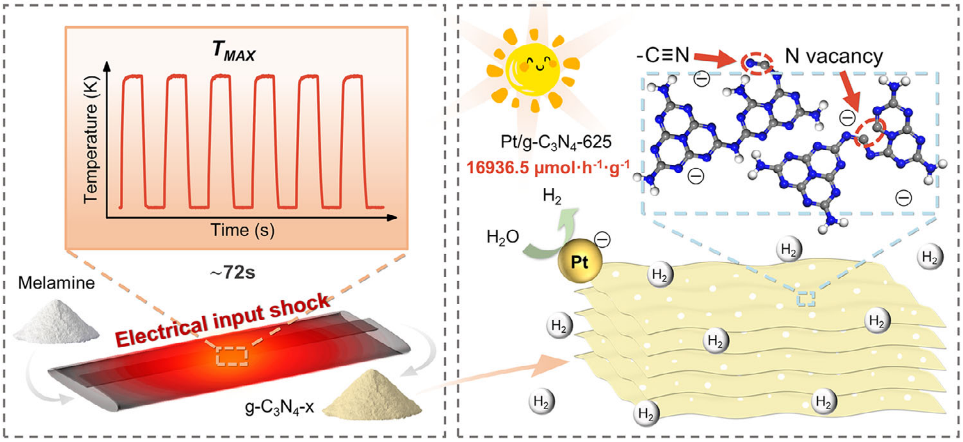

Figure 1. Concept image of the preparation of layered mesoporous nitrogen-defective carbon nitride with high-temperature impulse shock induced by flash Joule heating and its PHE.

precisely controlled within the range of 525–650 °C. Besides, detailed temperature evolution in one cycle of heating and cooling during flash Joule heating synthesis is displayed in Figure S1 (Supporting Information), which illustrates the changes in materials during high-temperature shock. Through iterative pulsed heating protocols, nitrogen-deficient carbon nitride nanostructures with tunable defect densities were synthesized in the form of powders, as evidenced by the morphological evolution presented in Figure 2a-III.

The $g\text{-}C_3N_4\text{-}x$ powders synthesized at different processing temperatures are depicted in Figure 2b. As the pulse processing temperature was increased, the color of the $g\text{-}C_3N_4\text{-}x$ powder changed from light grayish-yellow to dark earthy yellow because of changes in its bandgap.[30] Transmission electron microscopy (TEM) images revealed that the $g\text{-}C_3N_4\text{-}x$ produced by this method exhibits a well-defined lamellar porous structure (Figure S2, Supporting Information), with all samples exhibiting a uniform surface morphology. As displayed in Figure 2c,d, the prepared samples were rich in mesopores, which aligned with the results from Brunauer–Emmett–Teller (BET) analysis (Figure S3, Table S1, Supporting Information) and supported the presence of N_{2C} vacancies.[31]

To examine the effects of thermal processing parameters on the microstructures of carbon nitride, a series of $g\text{-}C_3N_4\text{-}x$ powder samples synthesized at varying temperatures were characterized and compared with commercial $g\text{-}C_3N_4$. X-ray diffraction (XRD) analysis (**Figure 3a**) and Fourier transform infrared (FTIR) spectroscopy (Figure 3b) revealed a high degree of similarity in microstructure between $g\text{-}C_3N_4\text{-}x$ and commercial $g\text{-}C_3N_4$, which confirms the successful synthesis through the flash Joule

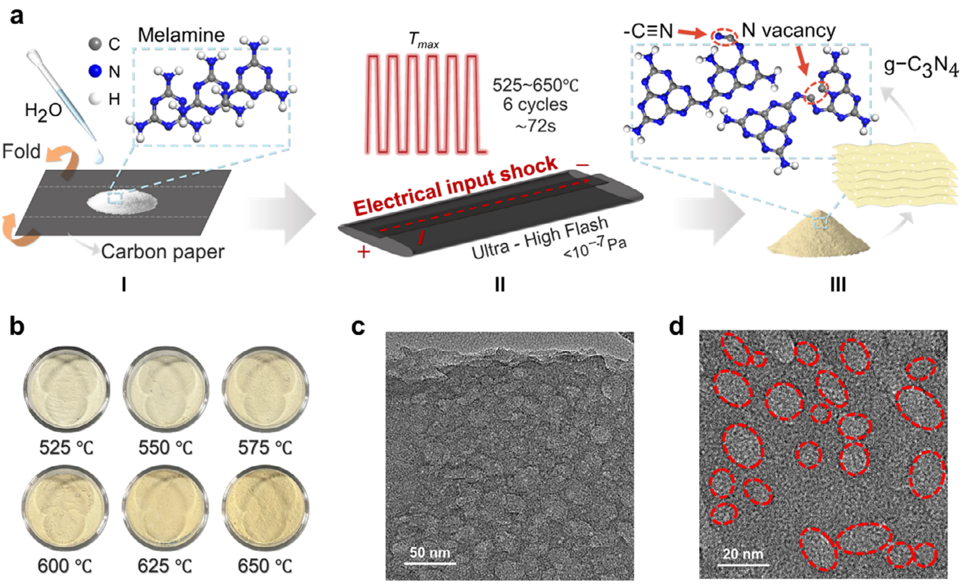

Figure 2. Schematic of the $g\text{-}C_3N_4\text{-}x$ processing procedure and its surface characteristics. a) Illustrated preparation. b) Color comparison of carbon nitride prepared at different high-temperature impulse shock conditions. c) TEM image showing the lamellar structure of $g\text{-}C_3N_4\text{-}625$, and d) surface mesopores.

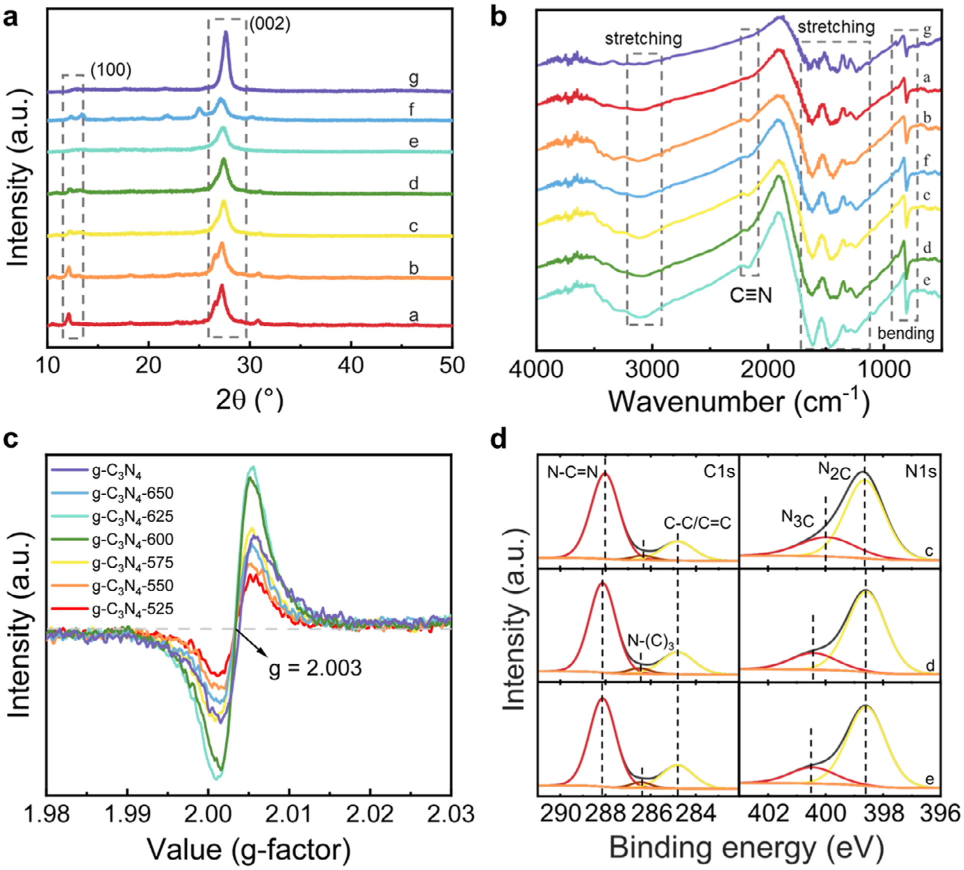

Figure 3. Microstructure characterization of g-C_3N_4-x. a) XRD patterns, b) FTIR spectra, c) EPR spectra, and d) C1s and N1s XPS spectra of g-C_3N_4-x (x = 525, 550, 575, 600, 625, 650) and g-C_3N_4. The labels a-g respectively correspond to g-C_3N_4-525, g-C_3N_4-550, g-C_3N_4-575, g-C_3N_4-600, g-C_3N_4-625, g-C_3N_4-650, and g-C_3N_4.

heating method. In the XRD pattern, commercial g-C_3N_4 exhibited two characteristic diffraction peaks at angles of 12.9° and 27.6°, which were respectively ascribed to the in-plane structural repetition in the (100) direction and the interlayer stacking in the (002) direction.[32] For g-C_3N_4-x, the (100) peaks shifted toward lower 2θ values as the processing temperature increased, indicating an increase in facet spacing that could result in a widened bandgap. The intensities of these peaks decreased as the processing temperatures increased, reflected a reduction in crystallinity and the introduction of structural defects. Notably, as the processing temperature increased, the (002) peak exhibited reduced intensity and a narrower half-peak width, and it shifted toward lower 2θ values, suggesting that the interlayer spacing decreased with an increase in the processing temperature, which enhanced the interlayer charge transfer rate.[32,33] Consequently, as the processing temperature increases under Joule heating, photocatalytic performance is expected to improve. A minor peak appeared at 25.1° in the XRD pattern of g-C_3N_4-650, suggesting that g-C_3N_4-650 underwent carbonization at 650 °C, which resulted in the structural transformation of its crystalline phase.[30,34] Furthermore, the XRD patterns of the g-C_3N_4 samples synthesized at 525 and 550 °C contained a distinct impurity peak at ≈30.8°, which could be attributed to the incomplete polymerization of heptazine units and their derivatives during the synthesis process. These results indicate that g-C_3N_4 remained in an atypical mixed structural phase before the complete formation of the g-C_3N_4 framework.[35] On the basis of these results, the 525–625 °C range is identified as the optimal processing temperature range for synthesizing g-C_3N_4-x using the flash Joule heating method.

The molecular structure and chemical bonding of the samples were investigated through FTIR spectroscopy as illustrated in Figure 3b. A prominent absorption band was observed at 800 cm^{-1}, which aligned with the theoretical predictions for s-triazine vibrations, while multiple peaks were observed within 1200–1600 cm^{-1}, which were attributed to the vibrational patterns associated with aromatic C—N heterocyclic units. The peak observed at ≈3100 cm^{-1} was ascribed to the stretching vibrations of N—H or O—H functional groups.[36,37] For samples synthesized at processing temperatures ranging from 550 to 650 °C, a weak absorption peak near 2170 cm^{-1} appeared, which was attributed to the asymmetric stretching vibration of cyano groups (C≡N),[38] the intensity of which increased progressively at higher impulse shock temperatures, indicating that elevated processing temperatures enhance the likelihood of additional C≡N defects forming in g-C_3N_4-x.

To further investigate the state of unpaired electrons within the samples, electron paramagnetic resonance (EPR) spectroscopy was performed on all samples (Figure 3c). For the g-C_3N_4-x samples synthesized via the flash Joule heating approach, a characteristic signal, which is associated with N vacancies, was observed near g of 2.003. This signal originated from the unpaired delocalized electrons that reside in the π-conjugated aromatic ring structure.[39] Moreover, the intensity of the EPR signals across the various samples was found to be directly proportional to the degree of defects observed in the FTIR spectra, indicating a clear correlation between the two characteristics.

To investigate the ontological structure and elemental composition of g-C_3N_4-x samples synthesized under various temperature-shock conditions, X-ray photoelectron spectroscopy (XPS) was employed. Elemental analysis revealed that as the processing temperature increased, a stepwise decrease in the N/C ratio commencing from 1.29, which is close to the theoretical value, to 1.04 (Table S2, Supporting Information), indicating the formation of nitrogen vacancies. Further insights were obtained through a detailed analysis of the C1s and N1s spectra (Figure 3d). The C1s spectra exhibited three peaks at ≈284.8, 286.4, and 288.0 eV, which were attributed to C═C or adventitious carbon, N-(C)$_3$, and hybridized carbons in N-containing aromatic rings, respectively.[40] A shift in binding energy to higher values with increasing pulse processing temperature suggested a rise in electron density, while a high-intensity peak at 286.4 eV confirms the formation of C≡N.[36] The N1s XPS spectra contained two distinct peaks, one at 398.6 eV and another at 400.4 eV, which were ascribed to nitrogen atoms in bi-coordinated (N_{2C}) and tri-coordinated (N_{3C}) configurations within the heptazine ring structure. The N_{2C} peak shifted to lower binding energies as the processing temperature increased, which is consistent with the fact that the binding energy of C≡N is lower than that of N_{2C}.[41] Moreover, the N_{2C}/N_{3C} ratio significantly decreased from 5.09 in g-C_3N_4-525 to 2.83 for g-C_3N_4-625, which suggested that the loss of N_{2C} occurred during the high-temperature impulse shock treatment preferentially,[13] with the absence of N_{2C} sites disrupted the charge balance and structural integrity of the heptazine framework, which leads to reduced crystallinity, as confirmed by FTIR and XRD analyses. From the direct comparison between g-C_3N_4-625 and g-C_3N_4 shown in Figure S4 (Supporting Information), it is evident that nitrogen defects have been effectively incorporated.

Investigations into the optical absorption properties and band structure of g-C_3N_4-x were carried out employing ultraviolet–visible diffuse reflectance spectroscopy (UV–vis DRS) and the valence band (VB) XPS. The samples synthesized at 625 °C exhibited stronger light absorption, with the maximum absorption wavelength being 456 nm (**Figure** 4a). However, no notable differences were observed in light absorption were observed among the other samples. The optical bandgap (E_g) for each sample was estimated by using Tauc plots (Figure 4b). The E_g for the g-C_3N_4-x (x = 525, 550, 575, 600, 625, 650) were calculated to be 2.59, 2.60, 2.56, 2.54, 2.52, and 2.58 eV for, with the commercial g-C_3N_4 serving as a comparison and exhibiting an E_g of 2.61 eV. To gain a clearer understanding of the effect of processing temperature on the electronic structure, the VB positions of all samples were analyzed using the following equation,[42]

$$E_{\mathrm{VB}} = \Phi + E_{\mathrm{VB-XPS}} - 4.44 \tag{1}$$

where Φ denotes the work function of the test instrument, which has a value of 4.2 eV. This allowed us to determine the VB position with respect to the normal hydrogen electrode at pH 7. The calculated VB minimum values for each sample, respectively, were 1.99, 1.96, 1.93, 1.85, 1.70, and 1.57 eV (Figure 4c). These findings reveal that the VB position of g-C_3N_4-x was influenced by the processing temperature, with a notable decrease from 1.75 eV for g-C_3N_4-525 to 1.33 eV for g-C_3N_4-650, suggesting a correlation between VB position and the presence of nitrogen defects. Combining the Tauc equation with the UV–vis DRS data, the conduction band maximum (CBM) for all samples was calculated, which respectively were −0.84, −0.88, −0.87, −0.93, −1.06, −1.25, and −0.85 eV. The introduction of nitrogen defects resulted in an overall negative shift in the CB of g-C_3N_4-x,[43] which closely mirrored the trend observed in the VB, and included a 0.41 eV more negative shift in the CB of g-C_3N_4-650 compared to g-C_3N_4-525 that is beneficial for photocatalytic activity.

To better visualize these findings, the energy band structures of the samples were explored (Figure 4d). The bandgaps of all the samples exhibited a decreasing trend within a specific temperature range, with g-C_3N_4-625 showing the smallest bandgap of 2.52 eV. Although g-C_3N_4-650 exhibited a slight increase in bandgap width, all g-C_3N_4-x samples had smaller bandgaps than the commercial g-C_3N_4. The presence of these defects was postulated to induce a mid-gap state through the overlap of the CB and VB, which further altered the bandgaps of the g-C_3N_4-x. Besides, these intermediate energy levels below the CB enable g-C_3N_4-x to absorb photons, which subsequently facilitates the excitation of electrons from VB to the defect state with lower energies, thus broadening the light absorption spectrum of g-C_3N_4-x and potentially enhancing its photocatalytic reduction capabilities. This suggests that these defects introduce mid-gap states that cause CB and VB to overlap, thereby changing the g-C_3N_4-x band-gap.[44] Additionally, acting as intermediate energy levels, these defects enable g-C_3N_4-x to absorb photons below the CB. Photon absorption initiates the electronic transition from VB to the defect state with lower energies,[38,45] thereby expanding the light absorption spectral range of g-C_3N_4-x and potentially enhancing its photocatalytic reduction capabilities.

The above characterization confirms that flash Joule heating can successfully introduce two types of nitrogen defects, including C≡N and nitrogen vacancies, and demonstrates their impacts on the microstructure and band structure. Cyano groups, which act as acceptors of free electrons, can enhance the efficacy of charge carrier transfer and separation,[46] whereas nitrogen vacancies inhibit charge carrier recombination.[47,48] The synergistic effect of these nitrogen defects is likely to influence charge carrier behavior.

To evaluate the effect of defect introduction via flash Joule heating on photogenerated electron-hole pairs recombination, photoluminescence (PL) emission spectrum analysis was performed on all samples (Figure 4e). Lower PL intensities correspond to reduced electron-hole recombination.[32] The results revealed that for all samples, except for g-C_3N_4-650, the PL peak intensity exhibited a decreasing trend with increasing pulse processing temperature, indicating that higher processing temperatures reduce sample crystallinity and inhibit carrier recombination. Among all samples, g-C_3N_4-625 exhibited the lowest PL peak intensity, suggesting that it had the best ability to suppress electron-hole

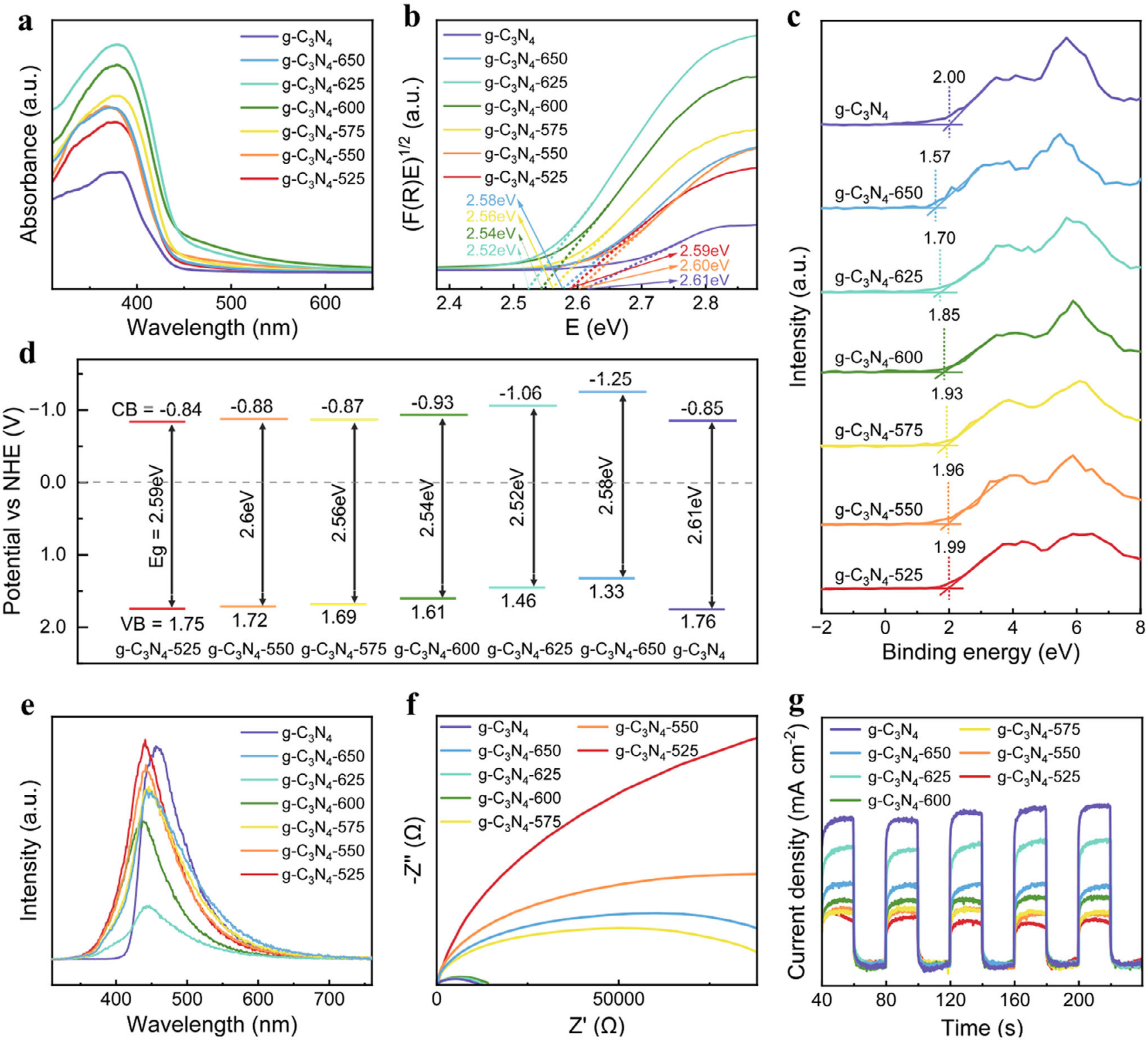

Figure 4. Band structure detection and photoelectric performance characterization of g-C_3N_4-x. a) UV–vis DRS image, b) plots of $(\alpha h\nu)^2$ versus the energy of absorbed light, c) VB-XPS image, d) band structure alignments, e) PL spectra, f) Nyquist plots from electrochemical impedance spectra, and g) photocurrent response of the photocatalysts of all samples.

recombination, which could be attributed to the defect trapping effect and the optimization of charge localization at terminal surface sites.[13] This finding was noted to be consistent with the results of other characterization analyses. In addition, the emission peak position in PL spectra typically reflects changes in the bandgap structure, which confirms that g-C_3N_4-x synthesized by flash Joule heating exhibits bandgap tuning compared to commercial g-C_3N_4. To assess the charge dynamics and charge mobility of samples processed at different temperatures, time-resolved photoluminescence (TRPL) measurements were performed. The results (Figure S5 and Table S3, Supporting Information) indicated that the average lifetimes (**Ave.**τ) ranged from 4.71 ns to 9.92 ns, with g-C_3N_4-625 exhibiting the shortest lifetime. This considerable reduction in the lifetime of photogenerated charge carriers was attributed to nitrogen defects enhancing the separation and transfer efficiency of excitons in g-C_3N_4-x.[49] Except for g-C_3N_4-650, the remaining samples exhibited a decrease in fluorescence lifetime with an increase in processing temperature. This suggests that the lifetime of photogenerated charge carriers is correlated with processing temperature, with this correlation being influenced by crystallinity and defect concentration. The defect states within g-C_3N_4-x can serve as non-radiative recombination centers, effectively trapping photogenerated electrons and holes,[50] thereby revealing a strong interdependence between the characteristics of defect states and the dynamics of charge recombination.[51] The g-C_3N_4-x samples prepared via flash Joule heating exhibit markedly suppressed photoluminescence (PL) intensity and shortened exciton lifetimes, indicating inhibited radiative recombination and the presence of efficient nonradiative pathways.[52] This behavior is typically attributed to defect-induced charge trapping associated with the introduced cyano groups and nitrogen vacancies as structural defects. Previous studies employing femtosecond transient absorption spectroscopy (fs-TAS) to probe the carrier dynamics provide further support for this mechanism. Nitrogen-related defects have been shown to function as localized separation centers,[53] accelerating nonradiative charge transfer by acting as electron traps and thereby suppressing radiative recombination.[54] Nitrogen vacancies introduce deep trap states that can rapidly capture photogenerated electrons, leading to quenched PL signals and reduced excited-state carrier lifetimes. In flash Joule heating, a rise in processing temperature results in additional non-radiative recombination pathways, thereby reducing the likelihood of radiative recombination in photogenerated charge carriers and consequently lowering the PL peak intensity. However, in light of the other characterization analyses and the final results, this effect remains less significant compared to the impact of crystallinity on the samples.

Electrochemical tests were conducted to assess the charge transfer and separation efficiencies of all samples (Figure 4f,g). Electrochemical impedance spectroscopy (EIS) was employed to assess the migration rate of photogenerated charges, and a Nyquist plot was used for this assessment, smaller semicircle radii represent lower charge transfer resistance and enhanced charge transfer ability.[55,56] The radii for the samples, except for g-C_3N_4-650, gradually decreased as the processing temperature increased indicating that resistance to photogenerated charge transfer decreased within a specific temperature range. These g-C_3N_4-625 and g-C_3N_4-600 exhibited radii that were akin to those of commercial g-C_3N_4, thus they had comparable efficiencies in promoting charge migration. Characterizations of the transient photocurrent response were also conducted to gain further insight into the rapid charge separation behavior of g-C_3N_4-x (Figure 4g).[57] Within a specific processing temperature range, the photocurrent signals increased with the processing temperature, this increase in intensity corresponded to an increase in the disintegration efficiency of electron-hole pair binding within g-C_3N_4-x. Compared with that of the other samples, the photocurrent intensity of g-C_3N_4-625 more closely resembled that of commercial g-C_3N_4, demonstrating that similar photogenerated charge separation efficiency between the two samples. These electrochemical results demonstrate that nitrogen defects introduced via flash Joule heating through high-temperature impulse shock heighten the PHE capabilities of g-C_3N_4-x by effectively amplifying its charge transfer capabilities. The increase in crystallinity of g-C_3N_4 plays a crucial role in facilitating electron transfer to the surface for chemical reactions.[58] In electrochemical tests, g-C_3N_4-x synthesized via flash Joule heating effectively introduces a higher concentration of defects, leading to a reduction in crystallinity. Consequently, although the bulk lattice of g-C_3N_4-x allowed for rapid charge migration, the interfacial ohmic contact resistance and disrupted electron transport pathways at the interface impeded electron transfer, resulting in g-C_3N_4-x exhibiting reduced charge transfer efficiency and electrochemical performance.[59] Compared with g-C_3N_4-x, commercial g-C_3N_4 had higher crystallinity and thus exhibited more efficient charge migration pathways in the bulk phase, thereby achieving superior electrochemical performance. Directional charge transfer is governed by a delicate balance between interfacial crystallinity and defect concentration.[60] Based on the comprehensive results from all photoelectrochemical performance tests, we conclude that g-C_3N_4-625, synthesized through flash Joule heating, represents a more favorable balance between defect states and crystallinity when compared to the other samples.

Compared with commercial g-C_3N_4, the g-C_3N_4-x prepared via flash Joule heating exhibits comparable photogenerated charge separation efficiency levels but demonstrated improved suppression of carrier recombination, which should expected to improve its photocatalytic performance. Nitrogen vacancies and cyano groups, which serve as crucial active centers for the PHE, contribute significantly to enhancing photocatalytic efficiency.[61] Accordingly, we conducted a series of PHE experiments, preparing photocatalysts were prepared by depositing 3.4 wt.% Pt atoms on each sample through the same method (**Figure 5a**), its average particle size is only 1.49 nm (Figure S6, Supporting Information). Upon exposure to visible-light, the catalytic response of the samples exhibited a volcano-like trend (Figure 5b), with g-C_3N_4-625 showing the superior hydrogen evolution rate achieving 16936.5 μmol h^{-1} g^{-1}, which is comparable to the leading benchmarks in the field (Table S3, Supporting Information). The photocatalytic activity of Pt/g-C_3N_4-650 decreased due to structural damage to g-C_3N_4-650 caused by excessive impulse shock temperatures, while the lower hydrogen evolution rates of carbon nitride prepared at lower impulse shock temperatures resulted from incomplete conversion of melamine.

Compared to the Pt-loaded g-C_3N_4 catalyst without nitrogen defects, Pt/g-C_3N_4-625 exhibited a catalytic activity that was 8 times higher (Figure 5c) and 16 times greater than that of g-C_3N_4-625 without Pt loading. Various characterization tests were conducted for Pt/g-C_3N_4-625 to investigate the effect of Pt loading on hydrogen evolution performance (Figure S7, Supporting Information). As displayed in Figure S7a (Supporting Information), the EPR signal of Pt/g-C_3N_4-625 was considerably stronger than that of g-C_3N_4-625, indicating that Pt coordinated with nitrogen vacancies and cyano groups to stabilize unpaired electrons and generate more paramagnetic centers.[40] Furthermore, Pt acted as an efficient electron sink and rapidly captured photogenerated electrons from g-C_3N_4-625, thereby effectively suppressing electron–hole recombination and causing a reduction in PL intensity (Figure S7b, Supporting Information).[62] To evaluate charge separation efficiency, we examined the EIS characteristics and photocurrent responses of g-C_3N_4-625 and Pt/g-C_3N_4-625.[63] The Nyquist plot obtained from the electrochemical impedance spectra of Pt/g-C_3N_4-625 (Figure S7c, Supporting Information) contained a smaller semicircle than did that obtained from the electrochemical impedance spectra of g-C_3N_4-625. This result can be attributed to the high-conductivity pathways provided by Pt and the Pt–N coordination with defects, which enhanced the conductive network of Pt/g-C_3N_4-625 and considerably reduced charge transfer resistance at the photocatalyst–electrolyte interface. Moreover, Pt loading enhanced charge carrier separation and transport efficiency by capturing photogenerated electrons and facilitating rapid interfacial charge transfer, thus partially mitigating the effect of low crystallinity on electron conduction

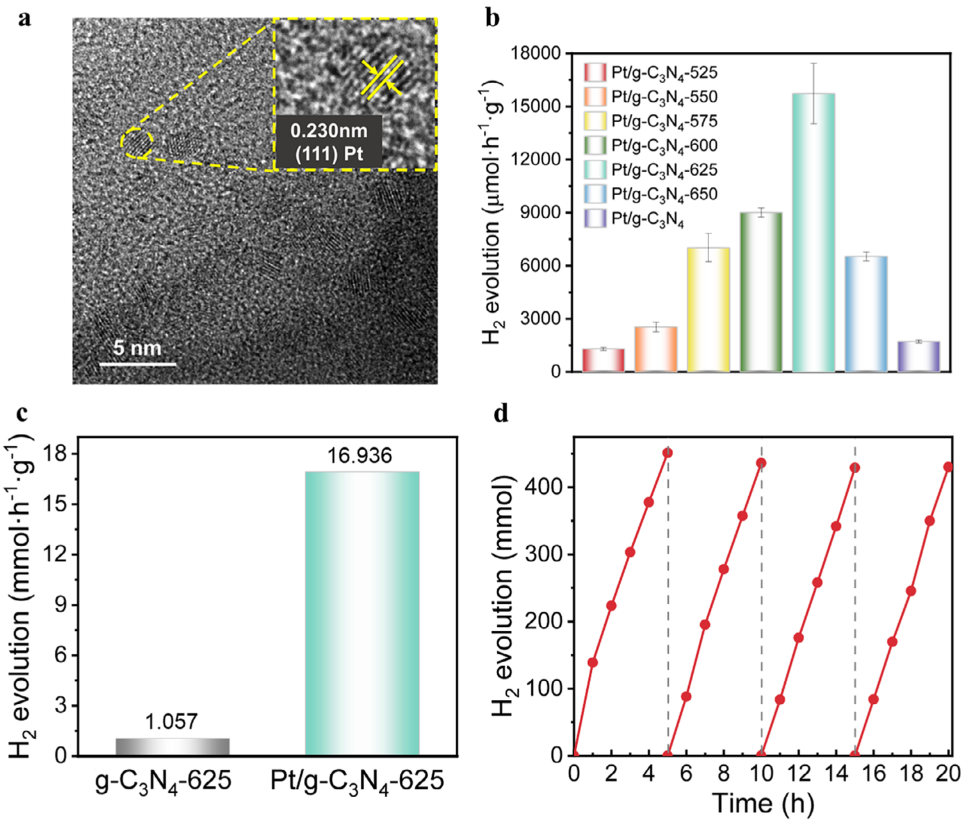

Figure 5. Characterization and performance evaluation of g-C_3N_4-x based photocatalysts with identical synthetic methodologies. a) Pt/g-C_3N_4-625 TEM image, with Pt deposited on the surface of g-C_3N_4-625. b) Hydrogen production rate diagram of Pt/g-C_3N_4-x (x = 525, 550, 575, 600, 625, 650). c) Comparison of hydrogen production rates between Pt/g-C_3N_4-625 and g-C_3N_4-625 without Pt. d) Stability test of Pt/g-C_3N_4-625 (Expressed as the total amount of H_2 evolved in each cycle).

and leading to an increased photocurrent (Figure S7d, Supporting Information). Furthermore, to systematically investigate the effect of Pt loading, we designed a linear concentration gradient system by preparing five chloroplatinic acid precursor solutions with progressively increasing concentrations. PHE experiments were then carried out under identical conditions using Pt/g-C_3N_4-625 samples derived from these solutions to preparation (Figure S7e, Supporting Information), which confirmed our sample had reached the maximum hydrogen evolution rate achievable under the current experimental setup. Although the other samples demonstrated lower hydrogen evolution rates than did the aforementioned sample, most of them still exhibited higher photocatalytic activities superior to that of Pt/g-C_3N_4, as a consequence of the elevated visible-light absorption and the nitrogen-defect-driven optimization of charge separation efficiency. These findings further confirm the beneficial role of nitrogen defects in enhancing photocatalytic performance.

Stability tests were also conducted for Pt/g-C_3N_4-625 (Figure 5d), and these tests indicated that the hydrogen evolution rate remained stable across four consecutive test cycles, with each test cycle lasting for 5 h each. This demonstrates that the introduction of nitrogen defects not only enhanced photocatalytic activity but also maintained structural stability, which is crucial for sustaining the performance of photocatalysts over long-term use in practical applications.

To further elucidate the mechanisms underlying the enhancement of optical absorption and charge separation, density functional theory (DFT) calculations were conducted for an idealized, pristine g-C_3N_4 monolayer, and for a defect-engineered system, g-C_3N_4-C≡N-V_N, which incorporates nitrogen vacancies and cyano functional groups as two distinct nitrogen-related defects. As shown in the calculated density of states (DOS) profiles (**Figure 6a,b**), the CB of pristine g-C_3N_4 was predominantly composed of C2p and N2p orbitals, whereas VB was primarily governed by N2p orbitals. These findings are consistent with those of previous research.[41] Moreover, the DOS plots revealed a noticeable bandgap narrowing of the bandgap in the defect-containing model, confirming that the incorporation of nitrogen defects plays a pivotal role in modulation.

The spatial distributions of the highest occupied molecular orbital (HOMO) and lowest unoccupied molecular orbital (LUMO) for g-C_3N_4 and g-C_3N_4-C≡N-V_N are presented in Figure 6c,d,f,g. In the pristine g-C_3N_4 system, the HOMO and LUMO had a relatively uniform distribution across the molecular framework. By contrast, in g-C_3N_4-C≡N-V_N, considerable charge density redistribution occurred, resulting in pronounced spatial separation between HOMO-localized holes and LUMO-localized electrons as well as the emergence of charge-enriched regions. This localized charge accumulation modified the electronic structure of g-C_3N_4-C≡N-V_N, leading to alterations in the VB

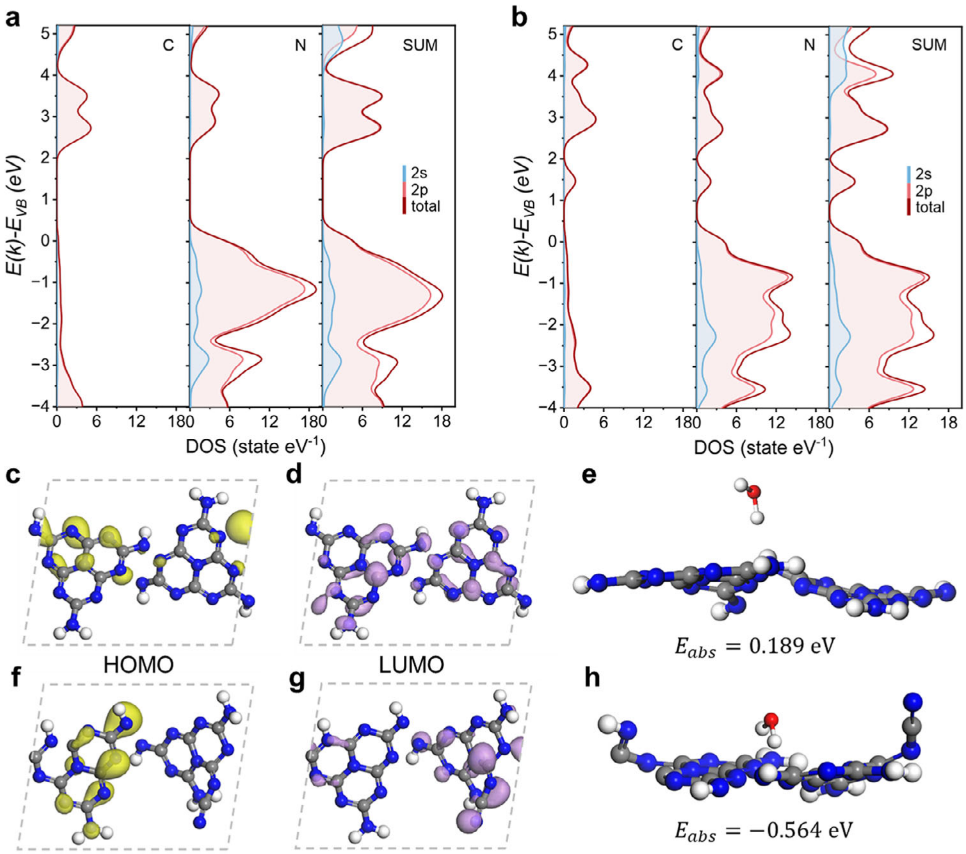

Figure 6. DFT simulation results for g-C_3N_4 and g-C_3N_4-C≡N-V_N. a,b) display the density of states (DOS) for g-C_3N_4 and g-C_3N_4-C≡N-V_N, respectively. c,d,f,g) respectively illustrate the charge density distributions of the highest occupied molecular orbital (HOMO) and the lowest unoccupied molecular orbital (LUMO) for g-C_3N_4 and g-C_3N_4-C≡N-V_N. e,h) respectively present the simulated snapshots of water molecule adsorption on the surfaces of g-C_3N_4 and g-C_3N_4-C≡N-V_N.

and CB edges and the formation of defect-associated mid-gap states.[64]

To explore the interaction of the interface with water molecules, we computed the adsorption energies of H_2O on the surfaces of g-C_3N_4 and g-C_3N_4-C≡N-V_N.[65] The simulated equilibrium adsorption configurations for g-C_3N_4 and g-C_3N_4-C≡N-V_N are displayed in Figure 6e,h, respectively, and the adsorption energies (E_{abs}) for these configurations were calculated to be 0.189 and −0.564 eV, respectively, indicating markedly higher water adsorption affinity in the g-C_3N_4-C≡N-V_N system than in the pristine g-C_3N_4 system.

3. Life Cycle and Technoeconomic Assessments

Flash Joule heating enables the rapid production of g-C_3N_4 samples with superior performance in a few seconds. By contrast, the commonly used thermal polymerization requires several hours to produce a batch of an equivalent quantity of carbon nitride. This extended processing time directly results in increased energy consumption and production costs.

To evaluate the advantages of flash Joule heating over thermal polymerization, we compared these methods' energy requirements, resource consumption, and environmental impacts through a life cycle assessment (LCA) and a cradle-to-gate technoeconomic assessment (TEA).[66] The comparative results are summarized in **Figure** 7a, as the consumption and emissions of carbon nitride prepared by flash Joule heating and thermal polymerization and a brief life cycle assessment of thermal polymerization of g-C_3N_4 with inputs and outputs are shown in Figures S8 and S9 (Supporting Information).

Flash Joule heating synthesis of carbon nitride uses melamine as the sole feedstock, which is mixed with water to form a paste, wrapped in carbon paper, and subjected to pulsed-shock processing in a reaction chamber to complete the synthesis. From an economic perspective, the cost difference between these methods is striking. Flash Joule heating synthesizes carbon nitride at just 2.04 ¥ kg^{-1}, far lower than the 25.8 ¥ kg^{-1} required by thermal polymerization (Figure 7b). The total energy consumption for this process is 8.57 MJ per kilogram of carbon nitride, with the flash Joule heating step consuming only 466.5 kJ (Figure 7c). In contrast, thermal polymerization consumes a total of 198.16 MJ for the same production scale. Although a marginally higher melamine conversion rate can be achieved in thermal polymerization than in flash Joule heating, thermal polymerization has a substantially higher energy demand. Besides, CO_2 emissions are a critical metric for assessing the environmental impact of these processes. The total CO_2 emissions for flash Joule heating are only 1311.4 g kg^{-1}, with the majority originating from melamine

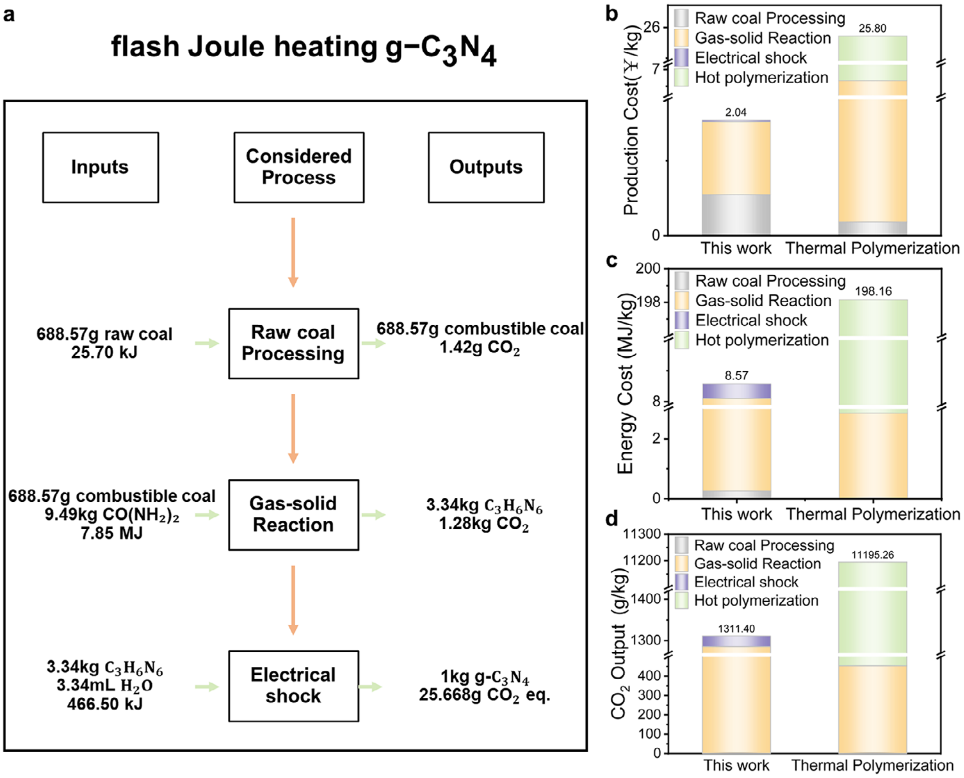

Figure 7. Life cycle assessment and economic benefit assessment analysis diagram. a) Brief life cycle assessment of flash Joule heating g-C_3N_4-x with inputs and outputs. b) Comparison of monetary costs, c) energy consumption, and d) CO_2 emissions for carbon nitride prepared by different methods, with some quantities being too small to be clearly visible in the graphs.

production. In comparison, the thermal polymerization generates 11195.26 g kg^{-1} of CO_2. Thus, thermal polymerization has a considerably higher environmental burden than flash Joule heating (Figure 7d). Considering energy efficiency, cost-effectiveness, and environmental friendliness, the flash Joule heating exhibits substantial promise for industrial-scale carbon nitride production. This approach not only reduces production costs and energy consumption but also mitigates environmental impact, thereby aligning well with the principles of sustainable development.

4. Conclusion

This study developed a novel flash Joule heating processing strategy for defect-modulating defects in g-C_3N_4. By leveraging the rapid heating and cooling characteristics of flash Joule heating, the method induces high-temperature shock, efficiently converting melamine into nitrogen-defective carbon nitride with a porous lamellar structure in an exceptionally short time (≈72s). This method facilitates the concurrent incorporation and meticulous regulation of two types of dual nitrogen-based defects encompassing in g-C_3N_4, namely nitrogen vacancies and cyano groups (C≡N). The resulting defect modulation helps optimize the band structure of g-C_3N_4, significantly enhancing its ability to suppress electron-hole recombination and dramatically improving its PHE activity. The Pt/g-C_3N_4-625 produced by the proposed method achieved an impressive hydrogen evolution rate of 16936.5 μmol h^{-1} g^{-1}, which is comparable to the leading benchmark catalysts for hydrogen production. Besides, this method demonstrates obvious advantages in cost-effectiveness and environmental sustainability, making flash Joule heating an economical, efficient, and eco-friendly approach to preparing high-performance nitrogen-defective g-C_3N_4 and related materials.

5. Experimental Section

Synthesis of Modified Graphitic Carbon Nitride g-C_3N_4-x: Melamine, 1 g, was put on the carbon paper, and an equal amount of deionized water was added so that they were fully mixed to form a mucilage, then the carbon paper was wrapped and folded and put into a high-temperature impact equipment, and the g-C_3N_4-x (x was the processing temperature of flash Joule heating, $x = 525, 550, 575, 600, 625, 650$) was obtained by using a 40 V pulse voltage and a strong pulse current of 200 A under the environment of the pressure of 10e-7 Pa, with high-temperature heating of 5 s and cooling of 5 s for 6 cycles.

Synthesis of Pt/g-C_3N_4-x (Pt Loading as 3.4wt.%): A chloroplatinic acid solution was obtained by dispersing 100 g of $H_2PtCl_6{\cdot}6H_2O$ in 1 mL of deionized water. The prepared g-C_3N_4-x of 150 g was placed on carbon paper, and 80 μL of the chloroplatinic acid solution was dropped into it to enable completely infiltrated the g-C_3N_4-x powder, and then Pt/ g-C_3N_4-x ($x = 525, 550, 575, 600, 625, 650$) was obtained by the same preparation.

Material Characterizations: X-ray diffraction (XRD) patterns of the powder were acquired utilizing a D8 ADVANCE diffractometer. FTIR spectra were generated with a Thermo Fisher Scientific Nicolet iS20 spectrometer. TEM and EDS analyses were conducted on samples using a JEOL JEM-F200, featuring a spherical aberration corrector. Room-temperature Electron Paramagnetic Resonance (EPR) spectra were captured with a Bruker EM4plus-6/1 spectrometer that matched the 300W Xe lamp with a full spectrum. XPS measurements and in situ, XPS analyses were performed using a Thermo Scientific K-Alpha spectrometer, which was equipped with an Al Kα X-ray source. Nitrogen adsorption–desorption isotherms were recorded at 150 °C using a Micromeritics ASAP 2460 gas adsorption analyzer. UV–vis diffuse reflectance spectra (DRS) and absorbance spectra were determined using a PerkinElmer Lambda950 spectrophotometer. Steady-state photoluminescence (PL) spectra were obtained using an Edinburgh Instrument FLS-1000 spectrometer at ambient temperature.

Electrochemical Tests: Electrochemical assays were conducted utilizing a CHI760E electrochemical workstation that employed a tri-electrode configuration. This setup comprised a platinum counter electrode, a silver/silver chloride reference electrode, and a fluorine-doped tin oxide (FTO) working electrode. For sample preparation, precisely 10 mg of the powdered specimen was measured and suspended in 1 mL of ethanolic solution. 20 µL of Nafion solution were incorporated subsequently, followed by ultrasonication for 30 min to achieve a uniform dispersion. Thereafter, 50 µL of this suspension was carefully applied to an FTO glass with an active component coating of 10 × 10 mm^2 and allowed to dry under ambient conditions.

Photocatalytic Hydrogen Evolution Test: Photocatalytic water splitting was conducted using a fully automated glass-based online trace gas analysis apparatus (Lab-solar-6A, Beijing Perfectlight). Illumination with visible light irradiation was simulated with a 300 W xenon lamp (PLS-S4E300+, Perfectlight) integrated with a 420 nm optical filter. Analysis of the off-gases was performed utilizing a gas chromatography system (GC-7900, Techcomp, China). For the reaction, 8.5 mg of Pt/g-C_3N_4-x photocatalyst was uniformly distributed within 100 mL of an aqueous medium comprising 10 vol% triethanolamine (TEOA). Before the reaction, the entire system was evacuated multiple times with nitrogen to ensure exhaustive air evacuation from both the solution and the reaction chamber. During the photocatalytic reaction, the sample was continuously stirred magnetically, and the reactor temperature was maintained at 10 °C using circulating water to eliminate thermal effects from the Xe lamp. The distance between the Xe lamp and the suspension surface was set to 10.0 cm. Evolved gases were collected at 1 h intervals and analyzed using a GC-7900 gas chromatograph, outfitted with a thermal conductivity detector (TCD), with nitrogen as the carrier gas. The volumetric production of hydrogen was ascertained by correlating the peak area with a predetermined calibration curve, derived from standard hydrogen gas measurements across a spectrum of known volumes. The photocatalytic stability was evaluated through cyclic tests over four cycles, with each cycle involving 5 h of total solar irradiation.

Computational Models and Methods: Calculations were performed using the CASTEP module in the Materials Studio software. A 2D melon sheet was constructed to simulate the incomplete polycondensation structure of melon, with a vacuum layer of 15 Å introduced to eliminate interactions between adjacent 2D sheets.[41] A cubic cell was employed to model the carbon nitride materials, adopting experimental lattice constants of $a = 7.8$ Å and $b = 13.6$ Å. To further suppress interlayer interactions, a large vacuum spacing of 15 Å was applied.

For geometry optimization, the generalized gradient approximation (GGA) with the Perdew–Burke–Ernzerhof (PBE) functional was used for describing the exchange–correlation energy in the DFT calculations. The plane-wave basis set was truncated with a cutoff energy of 400 eV, and the Brillouin zone was sampled using a 2 × 2 × 1 k-point mesh. The energy and force convergence thresholds were respectively set to 10^{-5} eV $atom^{-1}$ and 10^{-2} eV $Å^{-1}$. The adsorption energy (E_{abs}) of water molecules on the g-C_3N_4 and g-C_3N_4-C≡N-V_N surfaces was calculated as the difference between the total energy of the system with the water molecules positioned at equilibrium sites and the total energy when the water molecules were displaced 15 Å away from the surface.

Statistical Analysis: All the data in this manuscript were obtained through characterization tests and experiments. To ensure the comparability of data under different experimental conditions, all tests and experiments were conducted on samples from the same batch, using the same equipment, and measured/conducted in a concentrated time. For data involving mean values and standard deviations, the sample size for each statistical analysis was $n = 5$. All data calculations, analyses, and visualizations were completed using Origin 2024.

Supporting Information

Supporting Information is available from the Wiley Online Library or from the author.

Acknowledgements

This work was supported by the National Natural Science Foundation of China (grant No. 52422511, Y.C.), the Guangdong Basic and Applied Basic Research Foundation (grant No. 2022B1515120011, Y.C.), the Guangzhou Basic and Applied Basic Research Foundation (grant NO. 2024A04J6362, Y.C. and GZGX-24-01), and the Zhuhai Industry-University-Research Cooperation Project (grant No. 2320004002350, Y.C.).

Conflict of Interest

The authors declare no conflict of interest.

Author Contributions

J.X. was responsible for conceptualization, methodology, data curation, formal analysis, and writing of the original draft. Y.C. contributed to resources, funding acquisition, conceptualization, supervision, project administration, writing, reviewing, and editing. C.C. participated in the investigation, writing, reviewing, and editing. S.L. contributed to the investigation, validation, and data curation. L.C., J.Z., W.Z., Y.G., M.H., L.M., W.C., and X.C. were involved in the Investigation. C.-P.W. was responsible for supervision.

Data Availability Statement

Research data are not shared.

Keywords

flash Joule heating, g-C_3N_4, nitrogen defective, photocatalytic hydrogen evolution

Received: March 14, 2025
Revised: May 13, 2025
Published online:

[1] X. Wang, K. Maeda, A. Thomas, K. Takanabe, G. Xin, J. M. Carlsson, K. Domen, M. Antonietti, *Nat. Mater.* **2009**, *8*, 76.
[2] L. Lin, Z. Yu, X. Wang, *Angew. Chem., Int. Ed.* **2019**, *58*, 6164.
[3] Y. Ding, C. Wang, L. Pei, S. Maitra, Q. Mao, R. Zheng, M. Liu, Y. H. Ng, J. Zhong, L.-H. Chen, B.-L. Su, *Inorg. Chem. Front.* **2023**, *10*, 3756.
[4] H. Wang, J. Liu, R. Nie, Q. Shi, Q. Huang, T. Fukuda, *SmartBot* **2025**, *1*, 12007.
[5] J. Xu, Y. Li, S. Peng, G. Lub, S. Li, *Phys. Chem. Chem. Phys.* **2013**, *15*, 7657.
[6] P. Niu, G. Liu, H. Cheng, *J. Phys. Chem. C* **2012**, *116*, 11013.
[7] Z. Mo, X. She, Y. Li, L. Liu, L. Huang, Z. Chen, Q. Zhang, H. Xu, H. Li, *RSC Adv.* **2025**, *5*, 101552.
[8] C. Zhang, D. Qin, Y. Zhou, F. Qin, H. Wang, W. Wang, Y. Yang, G. Zeng, *Appl. Catal., B* **2022**, *303*, 120904.
[9] X. Yu, S. F. Ng, L. K. Putri, L. L. Tan, A. R. Mohamed, W. J. Ong, *Small* **2021**, *17*, 2006851.

[10] J. Li, K. Huang, Y. Huang, Y. Ye, M. Ziółek, Z. Wang, S. Yue, M. Ma, J. Liu, K. Liu, *J. Semicond.* **2023**, *44*, 81701.

[11] Z. Liang, Y. Xue, X. Wang, X. Zhang, J. Tian, *Mater. Today Nano* **2022**, *18*, 100204.

[12] F. Liu, J. Deng, B. Su, K.-S. Peng, K. Liu, X. Lin, S.-F. Hung, X. Chen, X. F. Lu, Y. Fang, G. Zhang, S. Wang, *ACS Catal.* **2025**, *15*, 1018.

[13] P. Niu, M. Qiao, Y. Li, L. Huang, T. Zhai, *Nano Energy* **2018**, *44*, 73.

[14] L. Liang, L. Shi, F. Wang, L. Yao, Y. Zhang, W. Qi, *Int. J. Hydrogen Energy* **2019**, *44*, 16315.

[15] J. Di, J. Xia, X. Li, M. Ji, H. Xu, Z. Chen, H. Li, *Carbon* **2016**, *107*, 1.

[16] Y. Zhang, J. Di, P. Ding, J. Zhao, K. Gu, X. Chen, C. Yan, S. Yin, J. Xia, H. Li, *J. Colloid Interf. Sci.* **2019**, *553*, 530.

[17] Z. Zhou, W. Guo, T. Yang, D. Zheng, Y. Fang, X. Lin, Y. Hou, G. Zhang, S. Wang, *Chin. J. Struc. Chem* **2024**, *43*, 100245.

[18] S. Panneri, P. Ganguly, B. N. Nair, A. A. P. Mohamed, K. G. K. Warrier, U. N. S. Hareesh, *Environ. Sci. Pollut. R.* **2017**, *24*, 8609.

[19] Y. Zhang, Z. Huang, C.-L. Dong, J. Shi, C. Cheng, X. Guan, S. Zong, B. Luo, Z. Cheng, D. Wei, Y.-C. Huang, S. Shen, L. Guo, *Chem. Eng. J.* **2022**, *431*, 134101.

[20] F. Lin, T. Wang, Z. Ren, X. Cai, Y. Wang, J. Chen, J. Wang, S. Zang, F. Mao, L. Lv, *J. Colloid Interf. Sci.* **2023**, *636*, 223.

[21] I. Y. Kim, S. Kim, S. Premkumar, J. H. Yang, S. Umapathy, A. Vinu, *Small* **2020**, *16*, 16136829.

[22] F. Longobardo, G. Gentile, A. Criado, A. Actis, S. Colussi, V. Dal Santo, M. Chiesa, G. Filippini, P. Fornasiero, M. Prato, M. Melchionna, *Mater. Chem. Front.* **2021**, *5*, 7267.

[23] T. Kubanaliev, Z. Eroglu, M. S. Ozer, O. Metin, *Catal. Sci. Technol.* **2023**, *13*, 2317.

[24] D. X. Luong, K. V. Bets, W. A. Algozeeb, M. G. Stanford, C. Kittrell, W. Chen, R. V. Salvatierra, M. Ren, E. A. McHugh, P. A. Advincula, Z. Wang, M. Bhatt, H. Guo, V. Mancevski, R. Shahsavari, B. I. Yakobson, J. M. Tour, *Nature* **2020**, *577*, 647.

[25] W. A. Algozeeb, P. E. Savas, D. X. Luong, W. Chen, C. Kittrell, M. Bhat, R. Shahsavari, J. M. Tour, *ACS Nano* **2020**, *14*, 15595.

[26] P. A. Advincula, D. X. Luong, W. Chen, S. Raghuraman, R. Shahsavari, J. M. Tour, *Carbon* **2021**, *178*, 649.

[27] Q. Dong, Y. Yao, S. Cheng, K. Alexopoulos, J. Gao, S. Srinivas, Y. Wang, Y. Pei, C. Zheng, A. H. Brozena, H. Zhao, X. Wang, H. E. Toraman, B. Yang, I. G. Kevrekidis, Y. Ju, D. G. Vlachos, D. Liu, L. Hu, *Nature* **2022**, *605*, 470.

[28] K. M. Wyss, R. D. De Kleine, R. L. Couvreur, A. Kiziltas, D. F. Mielewski, J. M. Tour, *Commun. Eng.* **2022**, *1*, 3.

[29] Yi Cheng, J. Chen, B. Deng, W. Chen, K. J. Silva, L. Eddy, G. Wu, Y. Chen, B. Li, C. Kittrell, S. Xu, T. Si, A. A. Martí, B. I. Yakobson, Y. Zhao, J. M. Tour, *Nat. Sustain.* **2024**, *7*, 452.

[30] A. Thomas, A. Fischer, F. Goettmann, M. Antonietti, J.-O. Müller, R. Schlögl, J. M. Carlsson, *J. Mater. Chem.* **2008**, *18*, 4893.

[31] X. Xu, Y. Xu, Y. Liang, H. Long, D. Chen, H. Hu, J. Z. Ou, *Mater. Chem. Front.* **2022**, *6*, 3143.

[32] G. Zhang, J. Zhu, Y. Xu, C. Yang, C. He, P. Zhang, Y. Li, X. Ren, H. Mi, *ACS Catal.* **2022**, *12*, 4648.

[33] G. F. S. R. Rocha, *Chem. Soc. Rev.* **2023**, *40*, 15.

[34] Y. Tang, J. Chen, X. Wang, X. Wang, Y. Zhao, Z. Mao, D. Wang, *Electrochim. Acta* **2019**, *324*, 134880.

[35] R. Vijayarangan, M. Sakar, R. Ilangovan, *J. Mater. Sci.: Mater. Electron.* **2022**, *33*, 9057.

[36] H. Cai, B. Wang, L. Xiong, G. Yang, L. Yuan, J. Bi, X. Yu, X. Zhang, S. Yang, S. Yang, *Chem. Eng. J.* **2020**, *394*, 124964.

[37] Q. Xu, B. Zhu, B. Cheng, J. Yu, M. Zhou, W. Ho, *Appl. Catal., B* **2019**, *255*, 117770.

[38] D. Zhang, Y. Guo, Z. Zhao, *Appl. Catal., B* **2018**, *226*, 1.

[39] J. Shen, C. Luo, S. Qiao, Y. Chen, Y. Tang, J. Xu, K. Fu, D. Yuan, H. Tang, H. Zhang, C. Liu, *ACS Catal.* **2023**, *13*, 6280.

[40] Q. Zhang, M. Yue, P. Chen, Q. Ren, W. Kong, C. Jia, Q. Lu, J. Wu, Y. Li, W. Liu, P. Li, Y. Fu, J. Ma, *J. Mater. Chem. C* **2023**, *12*, 3437.

[41] H. Yu, R. Shi, Y. Zhao, T. Bian, Y. Zhao, C. Zhou, G. I. N. Waterhouse, L.-Z. Wu, C.-H. Tung, T. Zhang, *Adv. Mater.* **2017**, *29*, 1605148.

[42] S. Trasa'tti, *Pure Appl. Chem.* **1986**, *58*, 955.

[43] W. Xing, C. Li, G. Chen, Z. Han, Y. Zhou, Y. Hu, Q. Meng, *Appl. Catal., B* **2017**, *203*, 65.

[44] M. Rezaei, A. Nezamzadeh-Ejhieh, A. R. Massah, *Energy Fuel.* **2024**, *38*, 8406.

[45] N. Zhang, X. Li, H. Ye, S. Chen, H. Ju, D. Liu, Y. Lin, W. Ye, C. Wang, Q. Xu, J. Zhu, Li Song, J. Jiang, Y. Xiong, *J. Am. Chem. Soc.* **2016**, *138*, 8928.

[46] G. Liu, G. Zhao, W. Zhou, Y. Liu, H. Pang, H. Zhang, D. Hao, X. Meng, P. Li, T. Kako, J. Ye, *Adv. Funct. Mater.* **2016**, *26*, 68226829.

[47] H. Dang, S. Mao, Qi Li, M. Li, M. Shao, W. Wang, Q. Liu, *Catal. Sci. Technol.* **2022**, *12*, 5032.

[48] J. Li, X. Wang, L. Huang, L. Tian, M. Shalom, C. Xiong, H. Zhang, Q. Jia, S. Zhang, F. Liang, *Nanoscale* **2021**, *13*, 12634.

[49] X.-X. Fang, L.-B. Ma, K. Liang, S.-J. Zhao, Y.-F. Jiang, C. Ling, T. Zhao, T.-Y. Cheang, A.-W. Xu, *J. Mater. Chem. A* **2019**, *7*, 11506.

[50] Y. Wang, P. Du, H. Pan, L. Fu, Y. Zhang, J. Chen, Y. Du, N. Tang, G. Liu, *Adv. Mater.* **2019**, *31*, 1807540.

[51] H. Zhuzhang, X. Liang, J. Li, S. Xue, Y. Lin, B. Sa, S. Wang, G. Zhang, Z. Yu, X. Wang, *Angew. Chem., Int. Ed.* **2025**, *64*, 202421861.

[52] H. Wang, L. Yu, J. Peng, J. Zou, J. Jiang, *J. Mater. Sci. Technol.* **2025**, *208*, 111.

[53] J. Zhang, G. Yang, B. He, B. Cheng, Y. Li, G. Liang, L. Wang, *Chin. J. Catal.* **2022**, *43*, 2530.

[54] X. Shi, M. Fujitsuka, S. Kim, T. Majima, *Small* **2018**, *14*, 1703277.

[55] X. Bai, L. Wang, Y. Wang, W. Yao, Y. Zhu, *Appl. Catal., B* **2014**, *152*, 262270.

[56] Y. An, Y. Tian, C. Liu, S. Xiong, J. Feng, Y. Qian, *ACS Nano* **2022**, *16*, 45604577.

[57] X. Zhou, X. Yu, L. Peng, J. Luo, X. Ning, X. Fan, X. Zhou, X. Zhou, *J. Colloid Interf. Sci.* **2024**, *671*, 134144.

[58] Y. Li, Z. Ren, Z. He, P. Ouyang, Y. Duan, W. Zhang, K. Lv, F. Dong, *Green Energy Environ.* **2024**, *9*, 623.

[59] X. Liu, B. Jing, G. Lun, Y. Wang, X. Wang, C. Fang, Z. Ao, C. Li, *Chem. Commun.* **2020**, *56*, 3179.

[60] J. Zhu, S. Wageh, A. A. Al-Ghamdi, *Chin. J. Catal.* **2023**, *49*, 5.

[61] V. W.-H. Lau, I. Moudrakovski, T. Botari, S. Weinberger, M. B. Mesch, V. Duppel, J. Senker, V. Blum, B. V. Lotsch, *Nat. Commun.* **2016**, *7*, 12165.

[62] E. C. Kohlrausch, H. A. Centurion, R. W. Lodge, X. Luo, T. Slater, M. J. L. Santos, S. Ling, V. R. Mastelaro, M. J. Cliffe, R. V. Goncalves, J. Alves Fernandes, *J. Mater. Chem. A* **2021**, *9*, 26676.

[63] Z. Zeng, Y. Su, X. Quan, W. Choi, G. Zhang, N. Liu, B. Kim, S. Chen, H. Yu, S. Zhang, *Nano Energy* **2020**, *69*, 104409.

[64] D. Zhao, C. L. Dong, B. Wang, C. Chen, Y. C. Huang, Z. Diao, S. Li, L. Guo, S. Shen, *Adv. Mater.* **2019**, *31*, 1903545.

[65] C. Wang, Y. Lu, Z. Wang, H. Liao, W. Zhou, Y. He, S. M. Osman, M. An, Y. Asakura, Y. Yamauchi, L. Wang, Z. Yuan, *Appl. Catal. B: Environ.* **2024**, *350*, 123902.

[66] L. Eddy, D. X. Luong, J. L. Beckham, K. M. Wyss, T. J. Cooksey, P. Scotland, C. H. Choi, W. Chen, P. A. Advincula, Z. Zhang, V. Mancevski, C. Kittrell, Y. Han, J. M. Tour, *Small Methods* **2024**, *8*, 2301144.